# Deformed vein sets as a record of synmetamorphic volume change: quantifying solution mass transfer in subduction-type metasediments of the Del Puerto Canyon region, Franciscan Belt, USA

SOEJIMA Shogo[1] and Wallis Simon Richard[2]

[1]University of Tokyo
[2]The University of Tokyo

November 16, 2022

## Abstract

The volume change component of deformation is often ignored or assumed to be zero in tectonic studies of metamorphic belts. However, when estimating original geometries of deformed regions, volume change is just as important as the other two components of deformation, finite strain and rotation. Major permanent volume change in metamorphic rocks is accomplished by solution transfer facilitated by flow of $H_2O$-rich fluids. Therefore, estimates of volume change can be combined with solubilities to estimate volumes of fluid flow. Previously applied methods for estimating rock volume change are based on estimates of absolute stretch, or changes in whole-rock chemical compositions. Estimates based on these approaches give large discrepancies even when applied to the same region. In this study, we develop a largely unexplored method for estimating volume change using the direction and deformation type of deformed mineral veins. The assumptions in this method are few and appropriate uncertainties can be estimated. Application of the new method to the metagreywacke in the Del Puerto Canyon of the Franciscan belt constrains the syn-metamorphic volume change to be greater than 7%, contrasting with previous proposals for large volume-loss in the same region. The results of previous studies can be modified taking into account grain rigid body rotation and grain boundary sliding. The final result of our approach yields a volume change of 7–21% vol.% and implies large amounts of water-rich fluid must have passed through the rock.

## Hosted file

`essoar.10510360.1.docx` available at https://authorea.com/users/523707/articles/595298-deformed-vein-sets-as-a-record-of-synmetamorphic-volume-change-quantifying-solution-mass-transfer-in-subduction-type-metasediments-of-the-del-puerto-canyon-region-franciscan-belt-usa

1

# Deformed vein sets as a record of synmetamorphic volume change: quantifying solution mass transfer in subduction-type metasediments of the Del Puerto Canyon region, Franciscan Belt, USA

S. Soejima[1] and S. R. Wallis[1]

[1]Department of Earth and Planetary Science, Faculty of Science, The University of Tokyo, Hongo 7-3-1, Bunkyo-ku, Tokyo, Japan 113-0033.

Corresponding author: Shogo Soejima (`s.soejima@eps.s.u-tokyp.ac.jp`)

Key Points:

- Analysis of deformed vein sets can be used to provide estimates of syn-metamorphic volume change associated with solution mass transfer.

- Volume change of metageywacke of the Franciscan terrane implies that large amounts of water-rich fluid must have passed through the rock.

Abstract

The volume change component of deformation is often ignored or assumed to be zero in tectonic studies of metamorphic belts. However, when estimating original geometries of deformed regions, volume change is just as important as the other two components of deformation, finite strain and rotation. Major permanent volume change in metamorphic rocks is accomplished by solution transfer facilitated by flow of $H_2O$-rich fluids. Therefore, estimates of volume change can be combined with solubilities to estimate volumes of fluid flow. Previously applied methods for estimating rock volume change are based on estimates of absolute stretch, or changes in whole-rock chemical compositions. Estimates based on these approaches give large discrepancies even when applied to the same region. In this study, we develop a largely unexplored method for estimating volume change using the direction and deformation type of deformed mineral veins. The assumptions in this method are few and appropriate uncertainties can be estimated. Application of the new method to the metagreywacke in the Del Puerto Canyon of the Franciscan belt constrains the syn-metamorphic volume change to be greater than 7%, contrasting with previous proposals for large volume-loss in the same region. The results of previous studies can be modified taking into account grain rigid body rotation and grain boundary sliding. The final result of our approach yields a volume change of 7–21% vol.% and implies large amounts of water-rich fluid must have passed through the rock.

1 Introduction

Determining the pre-deformation geometry of a geological terrane is one of the main goals of field-based structural geology. Such reconstructions require knowledge of all three components of finite deformation: strain, rotation, and volume change. Establishing methods for strain analysis applicable to rocks was one of the foundations of quantitative structural geology starting the 1960s (e.g. see summaries in Ramsay, 1967; Ramsay & Huber, 1983). Methods for estimating the rotational component have also been developed (e.g. Ghosh and Ramberg,

1976; Lister and Williams, 1983; Passchier, 1987; Passchier and Urai, 1988; Wallis, 1992; Wallis et al., 1993; Simpson and De Paor, 1993; Wallis, 1995; Tikoff and Fossen, 1995). The third parameter of finite deformation, volume change, has received much less attention and assessment of this component of finite deformation is commonly ignored or assumed to be negligible.

The lack of good constraints on the amount of syntectonic volume change in rocks is a major uncertainty in many balanced cross sections through orogenic belts that commonly assume constant area. Estimates of volume change of rock are also key to obtaining reliable estimates of crustal transport of soluble chemical species, such as $SiO_2$. $SiO_2$ in the form of quartz is both one of the most common minerals in the continental crust and has a high solubility in aqueous fluids. Crustal transport of $SiO_2$ in aqueous fluids may help control the bulk rock composition of the island arc crust (Breeding & Ague, 2002) and the recurrence interval of slow earthquakes (Audet & Burgmann, 2014). Significant fluid-mediated transport of $SiO_2$ should be reflected in volume decrease in its source domain and a volume increase in the sink domain. Despite the geodynamic importance of estimating syn-metamorphic volume change in metamorphic belts, current estimates are in many cases contradictory and generally lack good estimates of appropriate uncertainties.

In this study, we propose a geometric approach to volume change that is mainly based on analysis of deformed veins and apply this to the Franciscan metamorphic terrane of W USA. Veins are developed on a larger scale than most previously employed deformation markers and their analysis encompasses small scale processes such as grain boundary sliding. Our new analysis can be augmented by independent estimates of finite strain. Further constraints on volume change can be obtained by combining our results with grain-scale data.

1.1 Previous methods for estimating volume change in metamorphic rocks

Volume change of rocks during the stages of diagenesis and at relatively shallow levels can be assessed by changes in density and porosity (e.g. Wood 1974; Bray & Karig, 1985). Here, we focus on rocks from deeper levels that have experienced penetrative ductile deformation and in particular those where deformation by solution transfer processes is dominant. Such regions are commonly associated with the development of widespread slaty cleavage. Methods to estimate volume change in slates and other low-grade metamorphic rocks can be divided into geometric and geochemical approaches. Geometric approaches commonly indicate very large amounts of volume loss whereas geochemical studies commonly indicate small to negligible amounts of volume change.

Ramsay & Wood (1973) show that the deformed reduction spots of slate generally show a flattening or oblate shape. Assuming that the reduction spots were spherical before deformation and that deformation was plane strain (i.e., the absolute stretching of the middle axis of the strain ellipse was zero) implies volume loss of ~60%. An ingenious approach to estimating volume change was proposed by Wright & Platt (1982) who used graptolites to obtain information on absolute

stretching in slate rocks. Graptolites have a constant spacing between the thecae, so these fossils preserve information not only on the shape but also on the original dimensions: they act as millimeter-sized rulings embedded in the original pre-deformation rock. Using these properties Wright & Platt (1982) propose a volume loss of 50% during cleavage development in the Martinsburg Shale of the Appalachian orogen. A similar approach was used by Tan et al. (1995), but these workers included additional information on stretch derived from pressure shadows around framboidal pyrites and estimate a much smaller volume loss of the order of 5% in graptolite-bearing shales in the Gisborne area of Australia. Analysis of brittlely deformed conodonts contained within reduced spots of the Hamburg Slate in Shartlesville, central Pennsylvania yields an estimated volume loss of 29%–42% (Beutner & Charles, 1985). Analysis of worm-tubes and deformed veins with high effective viscosity ratios compared to the matrix, led Wright & Henderson (1992) to estimate a volume loss of 40–60% in the Goldenville Slate in Nova Scotia. Ring & Brandon (1999) use shapes of quartz grains and surrounding pressure shadows of metaclastic rocks in the Eastern Belt of the Franciscan Complex to estimate absolute stretching and proposed a volume reduction of up to 66%.

The most widely used geochemical approach to estimating volume change is based on the isocon method (Gresens 1968; 1986), which uses bulk rock chemical analysis and requires knowledge or assumptions concerning the original rock composition and immobile elements during deformation. Many studies that have applied this method to deformed slate yield roughly isovolumetric deformation throughout the rock body (e.g. Bhagat & Marshak 1990, Wintsch et al. 1991, Erslev & Ward 1994). A notable exception is reported by Kawabata et al. (2008), who use the isocon method to estimate volume loss of about 50% for metasedimentary rocks in the Shimanto Belt, southwest Japan.

The above summary shows the wide variety of different estimates of volume change. Some of the variability may be regional, but it is notable that methods based on geometric analyses tend to indicate large volume reduction whereas the geochemical isocon approach generally indicates much smaller volume change. The results suggest large unquantified uncertainties in the estimates.

In this study, we examine a different approach to estimating volume change based on geometric analyses of deformed mineral vein sets (e.g. Passchier, 1990; Wallis, 1992). The method we present is based on the recognition that with sufficient information on the deformation histories of material lines and their post deformation orientations it is possible to estimate all three components of finite deformation: volume change, strain, and rotation. This method requires few assumptions and has the potential to be a reliable tool for quantifying volume change in rocks but there are very few examples of it being applied to rocks and little study of associated uncertainties. Combining these results with estimates of finite strain and grain-scale analyses reported in previous studies of the same area allow us to further constrain the amount of volume change.

2 Theoretical background

3

2.1 Description of flow and deformation

The parameters of finite deformation of rock can be derived from steady flow parameters. Homogenous steady flow of rock can be described by the velocity gradient tensor $\boldsymbol{L}$ composed of nine components. In a rectangular coordinate system $X$, $\boldsymbol{L}$ is composed of the Euler velocity coefficients in the displacement equation (e.g. Malvern , 1969; Passchier, 1988).

$$\frac{dX_p}{dt} = \mathbf{L}_{pq} X_q \tag{1}$$

$\boldsymbol{L}$ can be described most simply by fixing the directions of the principle instantaneous stretching axes ($ISA_i$) of the flow to an external reference system. If $ISA_1$ indicates the direction of the maximum instantaneous stretch and $ISA_2$ indicates the direction of the minimum instantaneous stretch at 45° to $X_1$ and $X_2$ and the two ISA directions are fixed and perpendicular to $X_3$, $\mathbf{L}$ can be expressed by the following matrix (Malvern, 1969).

$$\mathbf{L} = \begin{bmatrix} a & s\,(1 + W_n) & 0 \\ s\,(1 - W_n) & a & 0 \\ 0 & 0 & s_3 \end{bmatrix} \tag{2}$$

We define $s_1$, $s_2$ and $s_3$ as the stretching rates along $ISA_i$, and s as the mean stretching rate in the $X_1$-$X_2$ plane: s = ($s_1$ - $s_2$) / 2. $W_n$ is a measure of the instantaneous non-coaxiality called the kinematic vorticity number. $W_n$ = 0 corresponds to pure shearing, and $W_n$ = 1 corresponds to simple shearing (Passchier, 1988). The average value of $W_n$ during the deformation period defines $W_m$, which is a parameter of finite deformation, and $W_n$ = $W_m$ in steady deformation. In addition, if a is the rate of area change then a = $s_1$ + $s_2$, and a = 0 for isoplanar flow. In this study we deal with plane strain flow that can be analyzed in two dimensions. In this case the associated two-dimensional flow in the $X_1$-$X_2$ plane is expressed by the 2 x 2 matrix

$$\mathbf{L} = \begin{bmatrix} a & s(1 + W_n) \\ s(1 - W_n) & a \end{bmatrix} \tag{3}$$

The deformation gradient (position gradient) tensor $\boldsymbol{F}$ is a tensor that relates the position $\boldsymbol{X}$ of the object point before deformation with the position $\boldsymbol{X}$ after deformation. And the tensor inverse position gradient tensor $\boldsymbol{H}$ has the opposite meaning.

$$\mathbf{X}' = \mathrm{FX} \ \text{ and } \ \mathbf{X} = \mathbf{HX}' \tag{4}$$

4

**F** is used to derive the position after deformation from the position before deformation, and **H** is used to derive the position before deformation from the position after deformation.

The incremental deformation gradient tensor $\mathbf{F_i}$ is obtained by time-integrating the velocity gradient tensor **L**.

$\mathbf{F}_i = \int \mathbf{L}\,\mathrm{d}t$

$$= \begin{bmatrix} a\,t & s\,t(1+W_n) \\ s\,t(1-W_n) & a\,t \end{bmatrix} + C$$

When $t = 0$, $\mathbf{F}_i = \boldsymbol{I}$

$$\mathbf{F}_i = \begin{bmatrix} 1+a\,t & s\,t(1+W_n) \\ s\,t(1-W_n) & 1+a\,t \end{bmatrix} \qquad (5)$$

The deformation gradient tensor $\mathbf{F}_f$ of finite deformation is derived from the following equation using $\mathbf{F}_i$.

$$\mathbf{F}_f = \lim_{\substack{t \to o \\ (n \bullet\ t = t)}} (\mathbf{F}_i)^n = \exp(\mathbf{L}t) \qquad (6)$$

This can be written as

$$\mathbf{F}_f = \begin{bmatrix} \exp(at) \bullet \cosh(st\sqrt{1-W_n^2}) & \frac{(1+W_n)\exp(at)}{\sqrt{1-W_n^2}}\sinh(st\sqrt{1-W_n^2}) \\ \frac{(1-W_n)\exp(at)}{\sqrt{1-W_n^2}}\sinh(st\sqrt{1-W_n^2}) & \exp(at) \bullet \cosh(st\sqrt{1-W_n^2}) \end{bmatrix}$$ (if $0 \le W_n \le 1$) (7)

(McKenzie,1979; Passchier, 1988).

One way to graphically represent a homogenous finite deformation field is to use a Mohr diagram (Fig. 1). Such representations are useful because they allow visual checks for possible mistakes in analysis and help determine when sufficient data have been collected. Despite their utility, such diagrams for finite deformation are not widely used. The main reason is probably because it has been thought the coordinates in Mohr space with the vertical axis $T_{ij}(i\,j)$ and the horizontal axis $T_{ij}(i=j)$ do not represent any physical aspect of deformation. However, as pointed out by Means (1982), the polar coordinates represent the stretch and rotation of the corresponding material line.

$\boldsymbol{F_f}$ can be plotted in Mohr space by defining two points on opposite sides of a diameter of the Mohr circle (Means, 1982, 1983). The diagonal components of the velocity gradient tensor and the incremental deformation gradient tensor are equal because the directions of $X_1$ and $X_2$ are fixed in directions where instantaneous elongation is related only to the rate of area change, which is represented by the same amount of stretching or shortening parallel to both

axes (equation 3 & 5). The diagonal components of the finite deformation gradient tensor are also equal (equation 7) because it can be expressed by powers of the incremental gradient tensor, so these two points are arranged in the vertical direction. Therefore, the parameters (Q, R, T, M and N) describing the Mohr diagram can be represented using the components of $\boldsymbol{F_f}$.

$$Q = \frac{F_{12} - F_{21}}{2} \tag{8}$$

$$R = F_{12} - Q = \frac{F_{12} + F_{21}}{2} \tag{9}$$

$$M = \frac{F_{11} + F_{22}}{2} = F_{11} = F_{22} \tag{10}$$

$$N = \sqrt{R^2 - Q^2} = \sqrt{F_{12}F_{21}} \tag{11}$$

and

$$T = \sqrt{M^2 + Q^2}$$

$$= \sqrt{F_{11}F_{22} + Q^2}$$

The determinant of $\boldsymbol{F_f}$ represents the area change rate, $\boldsymbol{F_f} = 1 + \Delta A$ (Ramsay & Huber, 1983) so:

$$T = \sqrt{1 + A + F_{12}F_{21} + Q^2} = \sqrt{(1 + A) + R^2} \tag{12}$$

From equations (7)-(12), the parameters of the finite deformation can be described using the parameters of the Mohr diagram. Here, $e_1$ and $e_2$ are maximum and minimum principal elongation along finite strain axes.

$$W_m = \frac{Q}{R} = \cos\theta \tag{13}$$

And, $1 + e_1 = T + R, \quad 1 + e_2 = T - R$ so:

$$R_s = \frac{1 + e_1}{1 + e_2} = \frac{T + R}{T - R} \tag{14}$$

$$1 + A = (1 + e_1) \bullet (1 + e_2) = T^2 - R^2 \tag{15}$$

Equations (13)-(15) show the usefulness of the Mohr diagram in estimating the three parameters of finite deformation.
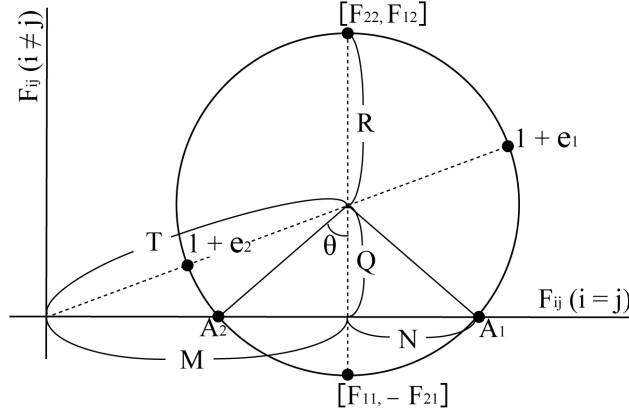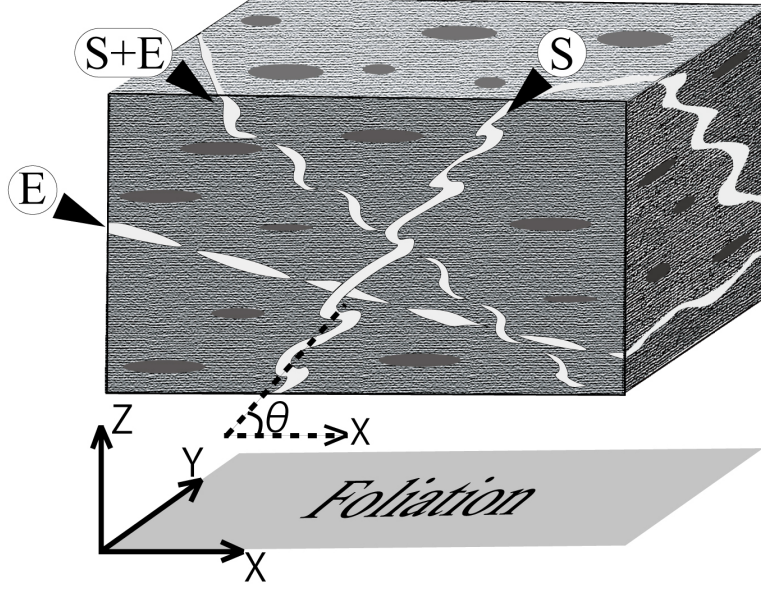


**Fig. 1.** Mohr diagram for $\mathbf{F_f}$. This diagram is read using polar coordinates, where the distance from the origin represents the stretch and the angle represents the rotation. The angle between lines represented by points on the circle is twice the angle measured in real space.

2.2 Construction of Mohr diagram from field data

A Mohr diagram for finite deformation can be derived using deformed vein sets (Passchier, 1990; Wallis, 1992). Deformed veins can generally be classified into three types: those showing only shortening (S-type), those showing only elongation (E-type), and those showing elongating after shortening (S + E-type). S-type veins are identified as folded veins, E-type veins are identified as necked or boudinaged veins, and S + E-type veins are identified as veins that have been boudinaged and then folded (Fig. 2). These different types of veins can be formed simultaneously during steady flow and their orientation ranges are determined by the deformation parameters. Lines representing the directions of the boundaries separating S-type from S + E-type veins and S + E-type from E-type veins are labeled as $L_{ai}$ and $L_{bi}$, respectively. $L_{ai}$ and $L_{bi}$ indicate the directions of the material lines that coincided with the directions of the lines separating the shortening direction and the extension direction of flow at the end of the deformation and at the start of the deformation, respectively. In other words, under steady flow, the material line that was oriented in the direction of $L_{ai}$ at the start of the deformation is oriented in the direction of $L_{bi}$ at the end of the deformation. Therefore, since the material line indicating the direction between $L_{ai}$ and $L_{bi}$ after the deformation is rotated from the shortening direction to the elongation direction of flow, it forms S + E-type veins. Material lines indicating directions between $L_{a1}$ and

7

$L_{a2}$ and between $L_{b1}$ and $L_{b2}$ form S-type and E-type veins, respectively. A Mohr diagram for deformation can be derived using the fact that the angle



between $L_{ai}$ and

$L_{bi}$ is equal to the angle through which $L_{bi}$ is rotated.

**Fig. 2.** Deformed veins can be divided into three types based on their shapes. The X-axis is parallel to the maximum finite extension direction, and the Z-axis is parallel to the minimum finite extension direction. The vein angle is measured counterclockwise in the XZ-plane in the direction that the vein extends relative to the X-axis.

When analyzing the deformation of a rock, it is generally the deformed state that can be observed and the original state must be estimated given the parameters of finite deformation. Therefore, the Mohr diagram for $\boldsymbol{H}$ is generally the most useful in geological studies. Here we summarize the procedure for drawing a Mohr diagram for $\boldsymbol{H}$ from the vein set data (Fig.3). The procedure follows Passchier (1992). The orientations of the material lines are represented by points on the Mohr circle for deformation. A central angle between two points on the Mohr circle is twice the angle in real space, so the two lines $L_{a1}$ and $L_{a2}$, which form angle in real space, are plotted as points 2 apart on the Mohr circle. In the Mohr diagram, the Mohr circle is placed in polar coordinates, and the distance from the origin to each point on the Mohr circle and the angle of each point measured from the abscissa represent the stretch of the line in that direction and the angle rotated during deformation, respectively. If the direction of the shortening and stretching regions of the rock flow did not change during the deformation (i.e. steady flow), the central angle of the S+E region is the angle

at which the line currently pointing in the direction of $L_{bi}$ rotated during the deformation. If the direction of the shortening and stretching regions of the flow did not change during the deformation (i.e. steady flow), the central angle of the S+E region is equal to the angle at which the line currently directed to $L_{bi}$ was rotated during the deformation. Thus, for example, $L_{b1}$ is located on the Mohr circle at an angle of 2 to $L_{a1}$, and at the same time at an angle of to the abscissa of the Mohr diagram. The drawing method to satisfy this is as follows. First the diagram is arranged so that $L_{a1}$ $L_{a2}$ is vertical. The angle on the Mohr circle is twice the angle in real space. Next, lines are drawn passing through $L_{b2}$ and perpendicular to $L_{a1}$ $L_{b2}$, and passing through $L_{b1}$ and perpendicular to $L_{a2}$ $L_{b1}$. The intersection of these lines is the origin of the Mohr diagram.

To make calculations of the deformation parameters, first the type and orientation of the veins on a specific surface of the rock are plotted on a circle, and the angles defined as $= L_{a1} \frown L_{a2}$, $= L_{a1} \frown L_{b1}$, and $= L_{b1} \frown L_{b2}$. Since these angles are doubled on the Mohr circle, if the Mohr circle is arranged so that $L_{a1}$ $L_{a2}$ is vertical, the slope of $L_{a1}$ $L_{b2}$, $k$, and the slope of $L_{a2}$ $L_{b1}$, $l$, are expressed as:

$$k = \frac{\{\sin\alpha - \sin(\alpha + 2\beta + 2\gamma)\}}{\{\cos\alpha - \cos(\alpha + 2\beta + 2\gamma)\}} \tag{16}$$

$$l = \frac{\{\sin(-\alpha) - \sin(\alpha + 2\beta)\}}{\{\cos\alpha - \cos(\alpha + 2\beta)\}} \tag{17}$$

If the coordinates of the center of the Mohr circle are (M, Q) and $L_{b1}(M + x_1, Q + y_1)$ and $L_{b2}(M + x_2, Q + y_2)$, the coordinates of the center of the Mohr circle in the Mohr diagram (M, Q) are represented as follows.

If $= 0$,

$$M = -\{x_2 + k(y_2 - y_1)\} \tag{18}$$

$$Q = -y_1 \tag{19}$$

If $\neq 0$,

$$M = -\frac{kl\left(\frac{x_1}{l} - \frac{x_2}{k} + y_1 - y_2\right)}{k - l} \tag{20}$$

$$Q = \frac{x_1 - x_2 + ly_1 - ky_2}{k - l} \tag{21}$$

If the radius of the Mohr circle is R,

$$L_{b1} = \begin{bmatrix} M + x_1 \\ Q + y_1 \end{bmatrix} = \begin{bmatrix} M + R\cos(\alpha + 2\beta) \\ Q + R\sin(\alpha + 2\beta) \end{bmatrix} \tag{22}$$

$$L_{b2} = \begin{bmatrix} M + x_2 \\ Q + y_2 \end{bmatrix} = \begin{bmatrix} M + R\cos(\alpha + 2\beta + 2\gamma) \\ Q + R\sin(\alpha + 2\beta + 2\gamma) \end{bmatrix} \tag{23}$$

$$N = \sqrt{R^2 - Q^2} \tag{24}$$

and

$$T = \sqrt{M^2 + Q^2} \tag{25}$$

Here, the kinematic dilatancy number $A$ is introduced (Passchier, 1990). $A$ represents the area change. If $A < 0$, the volume decreases, and if $A > 0$, the volume increases. The following equation holds for $A$.

$$A = \cos\alpha \tag{26}$$

and

$$A = \frac{M\ln(M)}{R} \qquad (if\ \beta\ =\ 0) \tag{27}$$

$$A = \frac{N\left\{\ln(M+N) + \ln(M-N)\right\}}{R\left\{\ln(M+N) - \ln(M-N)\right\}} \qquad (if\ \beta \neq\ 0) \tag{28}$$

$R$ is determined from the equation consisting of equation (26) and equation (27) or (28). With $R$ determined, the three parameters of the deformation are derived from equations (13)-(15).
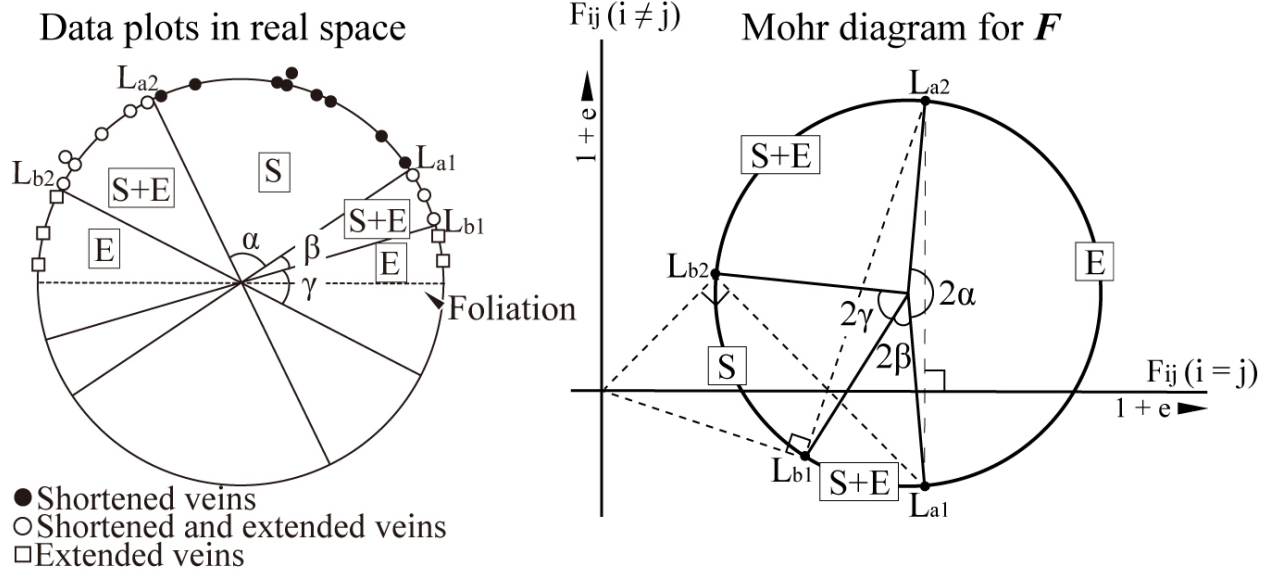
**Fig. 3.** Example of a plot of data from deformed vein sets. The left diagram shows the data of deformed vein sets measured in the field, and the right diagram is a Mohr diagram for $\boldsymbol{H}$ drawn based on the data. The plots on the left diagram are used to determine the angular range where different types of vein sets are distributed.

2.3 New Mohr diagram for analyzing field data

To construct a Mohr diagram for finite deformation, it is necessary to determine the directions of $L_{ai}$ and $L_{bi}$. However, information obtained from natural rocks can only constrain these orientations and not uniquely determine them. To incorporate uncertainties inherent in the data collected in the field, we present a modified approach to the way the Mohr diagram is constructed and presented, which we term a Variable-origin Mohr diagram (Fig. 4). This modification enhances our ability to perform quantitative analysis of rock deformation.

A normal Mohr diagram for finite deformation expresses deformation parameters through the position of its center and its radius (R). Therefore, to express appropriate uncertainties or errors in the estimates of the various deformation parameters, it is necessary to construct multiple Mohr circles with different positions and radiuses. This rapidly becomes an inconvenient way to display information and detracts from the utility of graphical representations. To simplify the expression of deformation parameters, we propose a Mohr diagram where the coordinates of the center of the Mohr circle and the radius are fixed but the location of the origin changes. The location of this origin defines the finite strain and rotation, and the volume change is expressed by the direction of the $L_a$ line on the Mohr circle. Therefore, in the Variable-origin Mohr diagram, it is possible to show a range of deformation parameters in a simple diagram.

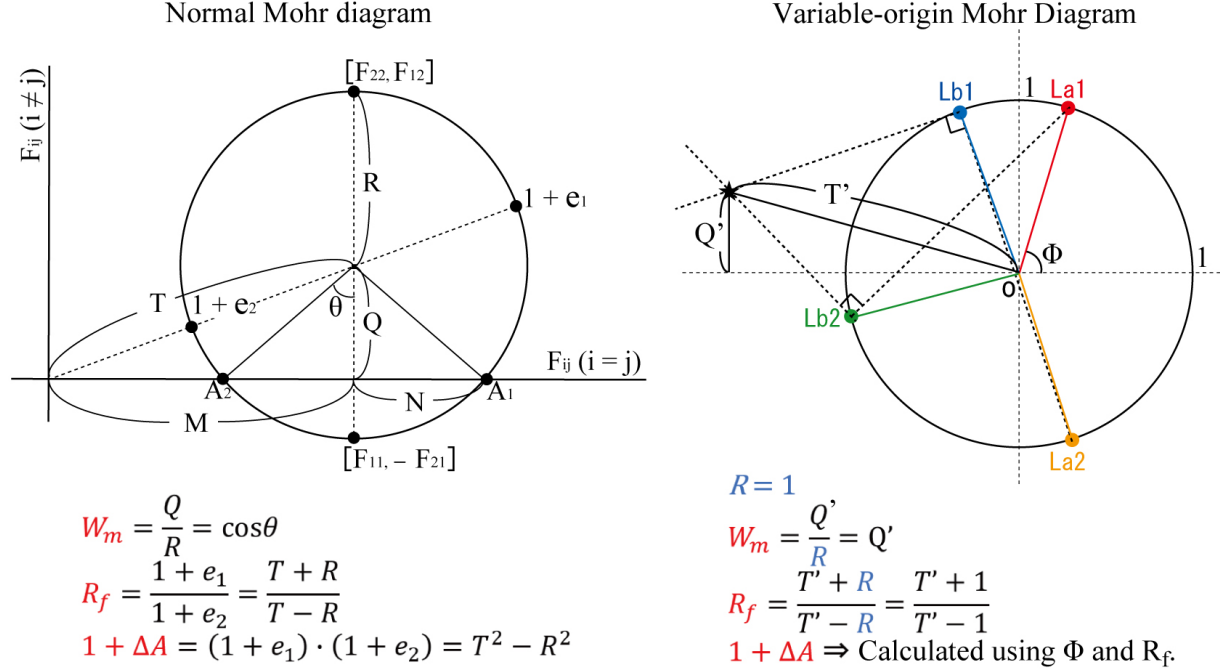A similar approach was proposed by Passchier (1993) to visualise progressive deformation or deformation paths.



**Normal Mohr diagram**

$$W_m = \frac{Q}{R} = \cos\theta$$

$$R_f = \frac{1 + e_1}{1 + e_2} = \frac{T + R}{T - R}$$

$$1 + \Delta A = (1 + e_1) \cdot (1 + e_2) = T^2 - R^2$$

**Variable-origin Mohr Diagram**

$$R = 1$$

$$W_m = \frac{Q'}{R} = Q'$$

$$R_f = \frac{T' + R}{T' - R} = \frac{T' + 1}{T' - 1}$$

$$1 + \Delta A \Rightarrow \text{Calculated using } \Phi \text{ and } R_f.$$

**Fig. 4.** The normal Mohr diagram and Variable-origin Mohr diagram. In the Variable-origin Mohr diagram, the origin of the polar coordinates is changed to the center of the circle, and the deformation parameters are represented by the positions of the plots indicated by the star.

The construction procedure for the Variable-origin Mohr diagram is as follows.

1) Draw a circle of radius 1 centered on the origin using a two-dimensional Cartesian coordinate system.

2) Plot the angular data of the deformed vein sets on the circle so that the points indicating the directions of $L_{a1}$ and $L_{a2}$ are aligned in the vertical direction. The angular data shown on the circle is twice the angle in real space, and the point indicating the direction of $L_{a1}$ is located in the upper half of the circle.

3) Plot the intersection point P of a line through $L_{b2}$ perpendicular to the line connecting $L_{a1}$ and $L_{b2}$ and a line through $L_{b1}$ perpendicular to the line connecting $L_{a2}$ and $L_{b1}$ on the figure.

The position of this point P represents the finite strain and the average vorticity. Specifically, the distance T' from the origin to point P is related to the finite strain $R_s$ by the following equation

$$R_s = \frac{T' + 1}{T' - 1} \tag{29}$$

and the vertical coordinate Q' of the point P is the mean vorticity number $W_m$ itself

$$W_m = Q' \ . \tag{30}$$

The remaining finite deformation parameter, the volume change $\Delta$V, is estimated using $\Phi$, which indicates the direction of $L_{a1}$ (the angle between $L_{a1}$ and $L_{a2}$ in real space), and the finite strain $R_s$. The specific estimation method is presented in the next section.

By incorporating the Monte Carlo statistical method, the Variable-origin Mohr diagram can also be used to represent appropriate uncertainties in the estimates of the deformation parameters that are estimated from the field data. The Monte Carlo method approximates the probability distribution of a solution by repeating a large number of analyses using random numbers. Random numbers are given for the $L_{ai}$ and $L_{bi}$ directions within the range constrained by the field data, and a point representing one deformation parameter per trial is plotted on the Mohr diagram. By repeating this trial tens of thousands of times, the range and probability distribution of the deformation parameter can be examined. When the random numbers are generated with a uniform distribution, a diagram can be derived that is suitable for examining the range of deformation parameters. When the random numbers are generated with a normal distribution, a diagram suitable for examining the probability distribution of the deformation parameters is obtained (Fig. 5). In the latter case, a confidence ellipse can be obtained from the distribution of points, allowing estimation of the deformation parameters, including error evaluation, from field data. When generating random numbers with a normal distribution, the range of angles in the $L_{ai}$ and $L_{bi}$ directions constrained by the field data is assumed to match the 99% confidence interval. The 95% confidence ellipse is then overlaid on a scatterplot of points showing the deformation parameters.
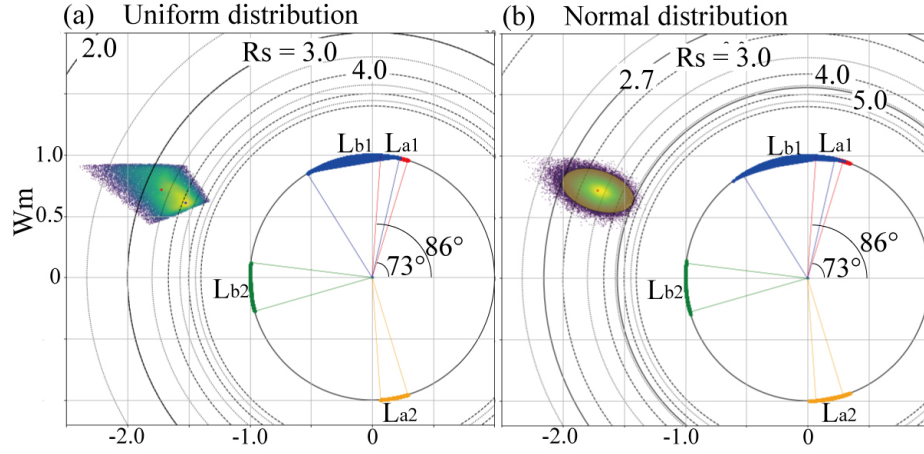
13

**Fig. 5.** Variable-origin Mohr diagram combined with the Monte Carlo method. (a) The Mohr diagram based on the uniform distribution represents the whole range of deformation parameters that can be accounted for by the vein sets data. (b) The Mohr diagram based on the normal distribution represents the probability distribution of the deformation parameters and allows for error evaluation.

2.4 Approximate estimation method of volume change

The graph shows the relationship between $\Phi$, which implies the angle between La1 and La2 in real space, and the volume change (Fig. 6). The graph shows that the effect of rotation $(W_m)$ is very small to negligible within the range of realistic volume changes possible for natural rock. Therefore, in order to investigate the range of possible values of volume change using the Variable-origin Mohr diagram, it is convenient to use the fact that the best estimate of volume change is dominantly dependent on the values of $R_S$ and $\Phi$ (angle between $L_{a1}$ and $L_{a2}$ in real space). The uncertainties due to the effect of rotation is minimized by using the best estimate of $W_m$ derived from the Variable-origin Mohr diagram.
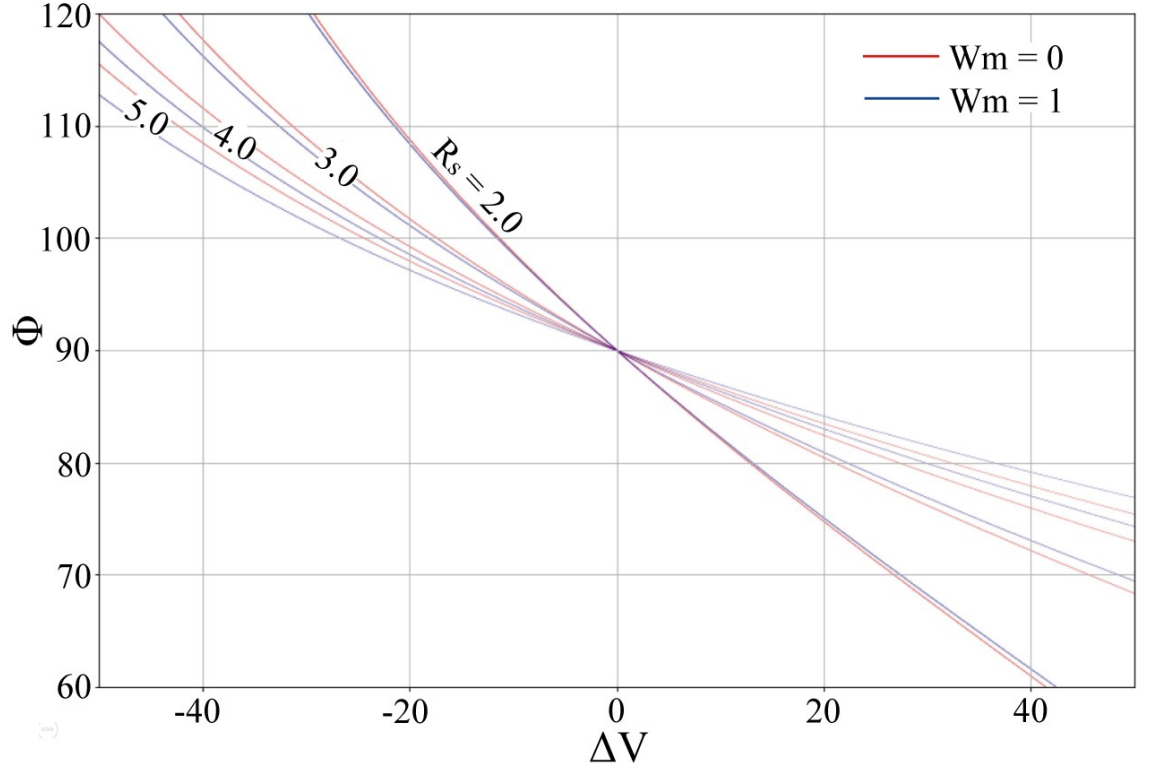
**Fig. 6.** The graph of the relationship between $\Phi$ and volume change at $R_S = 2.0$, 3.0, 4.0 and 5.0 when $W_m = 0$ (Red line) and $W_m = 1$ (Blue line).

The details of this method of estimating the volume change are as follows. The data required are finite strain ($R_S$), rotation ($W_m$) and $\Phi$. Normally, these data are not uniquely defined and have uncertainties. However, as mentioned above, since the effect of rotation ($W_m$) is very small when estimating the volume change, we can use the best estimate of Wm obtained from the analysis of the deformed vein sets. If $W_m$ is not known, we can adopt an intermediate value of $W_m = 0.5$ and any deviation will have only a small influence on the results. This means that if the ranges of finite strain ($R_S$) and $\Phi$ are known, the volume change can be estimated. To estimate the volume change, we use the following equations:

$$M = \left\{ T^2 - (W_m R)^2 \right\}^{\frac{1}{2}} \tag{31}$$

$$N = \left\{ R^2 - (W_m R)^2 \right\}^{\frac{1}{2}} \tag{32}$$

$$T = \frac{R(R_s + 1)}{R_s - 1} \tag{33}$$

$$\frac{N\left\{\ln\left(M + N\right) + \ln(M - N)\right\}}{R\left\{\ln\left(M + N\right) - \ln(M - N)\right\}} = \cos\Phi \tag{34}$$

By solving these simultaneous equations, we can obtain R as a function of $R_S$, $W_m$ and $\Phi$. Since one representative value is used for $W_m$, R is treated as a function of $R_S$ and $\Phi$. R is related to the volume change ($\Delta V$) by the following equation:

$$V = T^2 - R^2 - 1 = \left\{\left(\frac{R_f + 1}{R_f - 1}\right)^2 - 1\right\} R^2 - 1 \tag{35}$$

Therefore, the volume change is derived as a function of $R_S$ and $\Phi$. The minimum and maximum values of the estimated volume change are determined by the combination of the minimum ($R_{Smin}$) or maximum ($R_{Smax}$) estimates of $R_S$ and the minimum ($\Phi_{min}$) or maximum ($\Phi_{max}$) estimates of $\Phi$. These relationships can be shown in graphs showing the relationship between $\Phi$ and $\Delta V$ at $R_{Smax}$ and $R_{Smin}$ (Fig. 7).
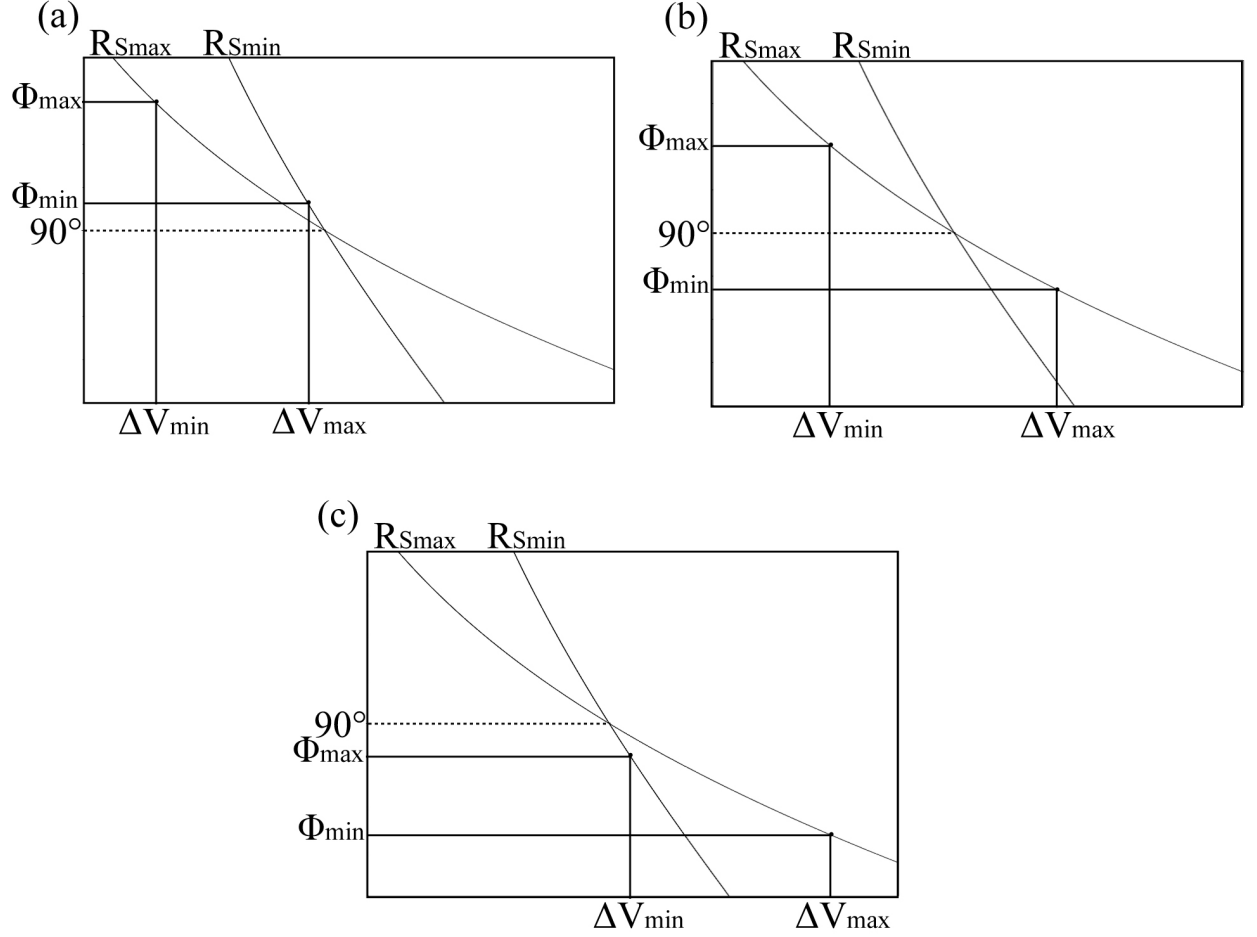
**Fig. 7.** The graph showing the relationship between $\Phi$ and $\Delta V$ at $R_{Smax}$ and $R_{Smin}$ . (a) $90° < \Phi_{min} < \Phi_{max}$. (b) $\Phi_{min} < 90° < \Phi_{max}$. (c) $\Phi_{min} < \Phi_{max} < 90°$.
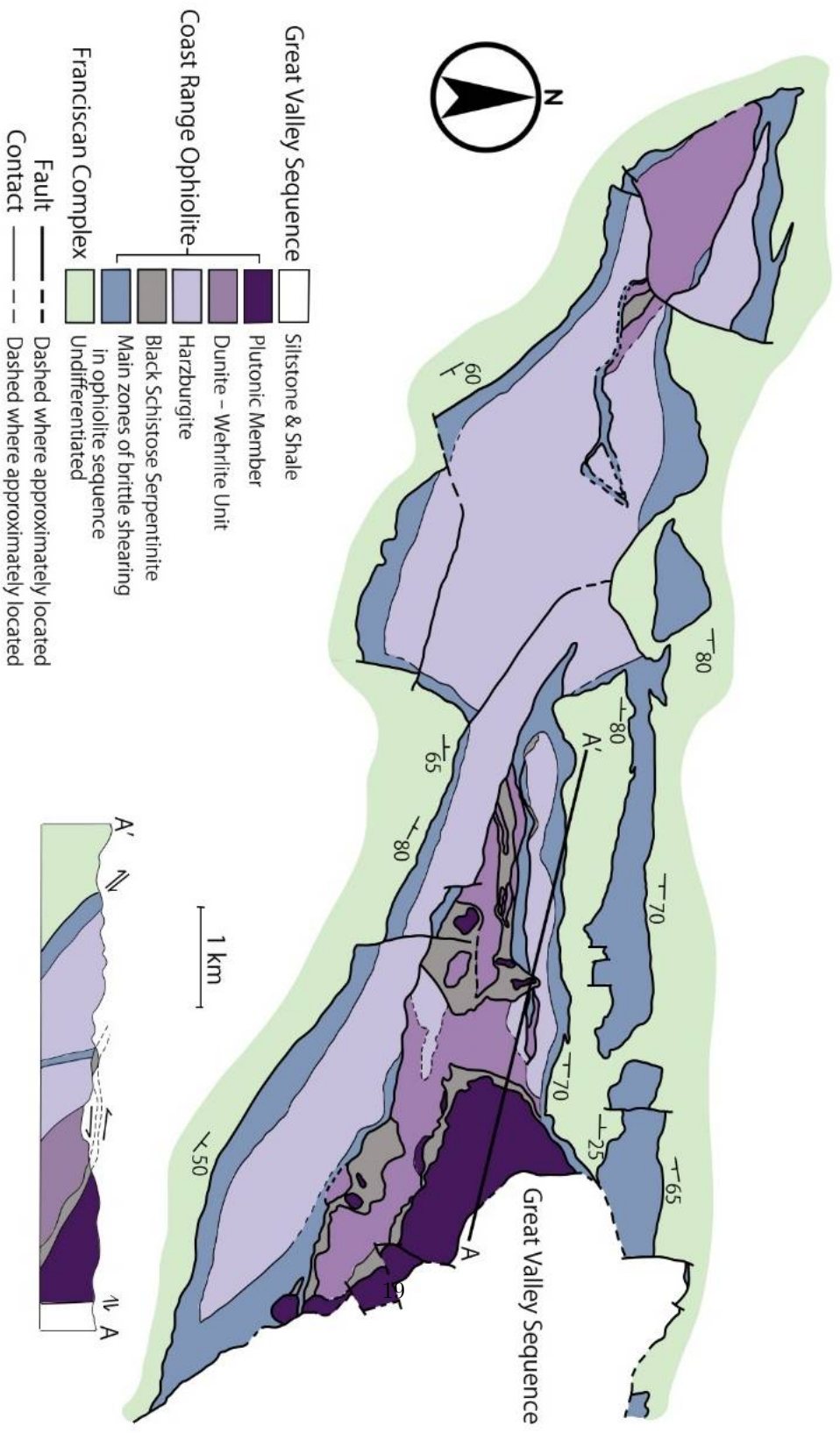
## 3 Application to field data

### 3.1 Geological background

As a real example, in this study, we estimated the deformation parameters including the volume change of metagraywacke from Del Puerto canyon in the Franciscan belt in the western United States. The study area is about 10 km east-west and 5 km north-south along the Del Puerto canyon, about 40 km east of San Jose, California (Fig. 8).

Metagraywacke that has undergone subduction metamorphism is distributed throughout this study area. The development of a strong foliation indicates the region has undergone high-strain deformation. Only one phase of ductile

deformation was identified. The foliation is associated with well-developed selvages of opaque minerals and. In addition to lithic fragments, clastic grains of quartz and feldspar are common. Microstructural observations show the clastic grains are associated with pressure fringes of quartz and there is only limited evidence for dislocation creep and dynamic recrystallization (see also Ring, 2008). These features suggest the dominant deformation mechanism is solution transfer. Previous studies by Ring (2008) have used grain shapes and analyses of the pressure fringes to suggest the metagreywake of this area has undergone large syn-metamorphic volume decrease of about $-30\%$.

Minerals veins are commonly developed within the metagraywacke. These veins are typically 1–10 mm thickness and are developed in various directions. These veins dominantly consist of quartz although other minerals including key high-P metamorphic minerals such as lawsonite are also present (Fig. 9). The mineral assemblage of these veins suggests that they formed during or close to the peak of high-pressure metamorphism and the deformation should reflect deformation close to peak burial depth and including part of the subsequent exhumation processes. In this study, finite strain analysis was performed using both the deformed vein sets method described in detail here and the $R_f$ / method (e.g. Ramsay 1967; Lisle 1985) applied to clastic rock fragments and grains.
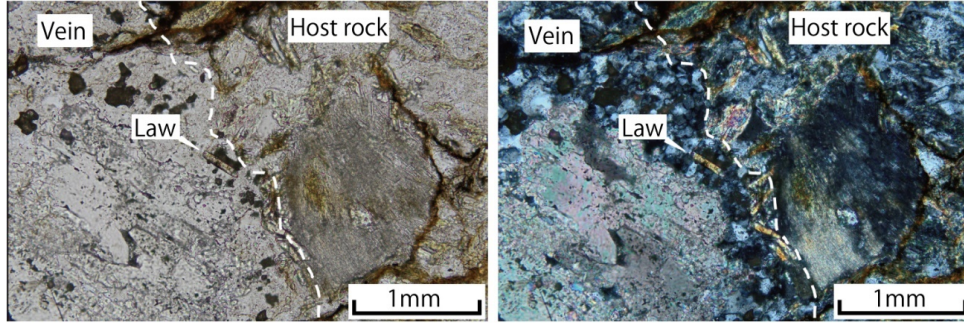
N

Great Valley Sequence
Siltstone & Shale

Coast Range Ophiolite
Plutonic Member
Dunite – Wehrlite Unit
Harzburgite
Black Schistose Serpentinite
Main zones of brittle shearing
in ophiolite sequence
Undifferentiated

Franciscan Complex

Fault — Dashed where approximately located
Contact — Dashed where approximately located

60
80
65
80
70
70
25
65
50

A
A'

1 km

Great Valley Sequence

Great Valley Sequence

**Fig. 9.** Photomicrograph of lawsonite-bearing quartz vein.

3.2 Strain analysis by $R_f$ / method

The axial ratio $R_f$ after deformation of an elliptical strain marker in a rock and the angle that its major axis makes from an appropriate reference plane can be used to estimate the axial ratio $R_i$ of the marker before deformation and the axial ratio of the actual strain ellipse $R_S$. This method is called the $R_f$ / method (e.g. Ramsay, 1967). A development of the $R_f$ / method proposed by Lisle (1985) allows estimation of the uncertainties based on the $\chi^2$ test. In this contribution, the Greek letter 'phi' is already used in the discussion of the geometric analysis of veins. To distinguish the two uses we use the lower-case letter ' ' when referring to the angles used in the strain analysis. In this study, quartz particles and sandstone fragments in metagraywacke were used as strain markers and analyzed by the $R_f$ / method. The samples used for the analysis were obtained from two different sites (DP3 & 98DP5 on Fig. 10), and strain analyses were performed on each sample using both quartz particles grains and sandstone fragments. The results of the analysis are presented in Table 1. Samples from both locations show similar results. In general, the sandstone fragments show about 10% greater shortening in the Z-axis than the quartz particles.
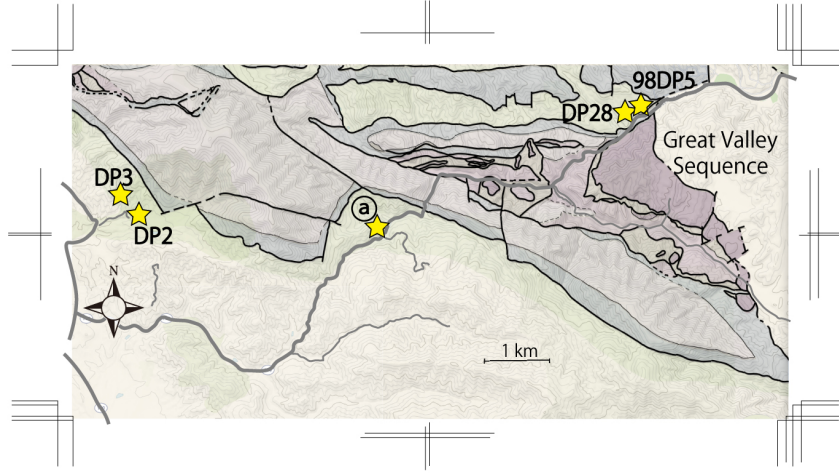
20

**Fig. 10.** Locations where sampling and deformed vein mesurments were taken. The thick gray lines represent Del Puerto Canyon Road (Route 130), and the thin gray lines represent forest roads, etc. The geological map is overlaid on the topographic map.

**Table 1.** The results of the $R_f$ / analysis. $R_S$ represents the axial ratio of the strain ellipse and indicates the range that is statistically compatible with the data at the 5% significance level. *Indicates the value with the maximum likelihood.

| Sandstone fragments | | | | | |
|---|---|---|---|---|---|
| Sample | Grain size (mm) | Rs | Rs* | Shortening in Z-axis (%) | Shortening in Z-axis |
| DP3 | 2–15 | 3.2–4.0 | 3.7 | 44–50 | 48 |
| 98DP5 | 5–20 | 3.3–4.6 | 4.0 | 45–53 | 50 |
| **Quartz particles** | | | | | |
| Sample | Grain size (mm) | Rs | Rs* | Shortening in Z-axis (%) | Shortening in Z-axis |
| DP3 | 0.2–1.0 | 2.4–3.0 | 2.7 | 35–42 | 39 |
| 98DP5 | 0.2–1.0 | 2.7–3.2 | 2.9 | 39–44 | 41 |

3.3 Estimation of the shape of grains before deformation using the $R_f$ / method

In addition to estimating the finite strain, $R_S$, the $R_f$ / method can also be used to estimate the aspect ratio before deformation $R_i$. However, because the method was established with the aim of estimating $R_S$, uncertainties are generally only considered for $R_f$, e.g. the Theta-Curve method (Lisle, 1985; Moriyama & Wallis, 2002), and Hyperbolic vector mean method (Yamaji, 2008). In this study, we used the bootstrap method to estimate the uncertainty of $R_i$. The bootstrap method is a technique for estimating the statistical properties

of the true population from the statistical values of each sample by considering the sample data as a pseudo-population and repeatedly resampling (1000–2000 times or more), allowing for overlap. In this study, we used this method to estimate the statistical properties of the mean aspect ratio of quartz grains before deformation in this region.

In the $R_f$ / method, the aspect ratios, $R_f$, are plotted against directions, , of the major axis of the grains after deformation. If the aspect ratios of all grains before deformation are equal, the $R_f$ / plots after deformation will lie on a single closed curve expressed by the following equation (Lisle, 1985).

$$\cos 2\varphi = \frac{\left(R_f + 1/R_f\right)\left(R_s + 1/R_s\right) - 2(R_i + 1/R_i)}{\left(R_f - 1/R_f\right)\left(R_s - 1/R_s\right)} \tag{36}$$

Therefore, $R_i$ of each grain can be calculated from the data of each grain ($R_f$ and ) and the result of the Theta-Curve method ($R_S$). The $R_i$ data for all grains are used as sample data for the bootstrap method. Then, we obtained the mean $R_i$ for each bootstrap sample (BS sample), and from the resulting distribution, we estimated the probability distribution of the mean $R_i$ of the population. According to the central limit theorem, regardless of the distribution of the original data, the distribution of the mean of the BS sample approaches a normal distribution as the number of trials increases (Lindeberg, 1922 ), so the probability distribution of the estimated mean $R_i$ can be approximated to a normal distribution. We also used this information to examine the implied uncertainties for the estimates of volume change given by Ring (2008). We used published data from 16 samples from the same Del Puerto Canyon as used for the vein analysis presented in this study. The mean and standard deviation of $R_i$ for DP3 were found to be 1.45 and 0.03, respectively, and those for 98DP5 were found to be 1.34 and 0.04, respectively. Therefore, the mean aspect ratio of the quartz particles in this region before deformation was up to about 1.5. The associated mean and standard deviation for volume change implied by the method of Ring (2008) are then $-22\%$ and $4\%$, respectively (Fig. 11).
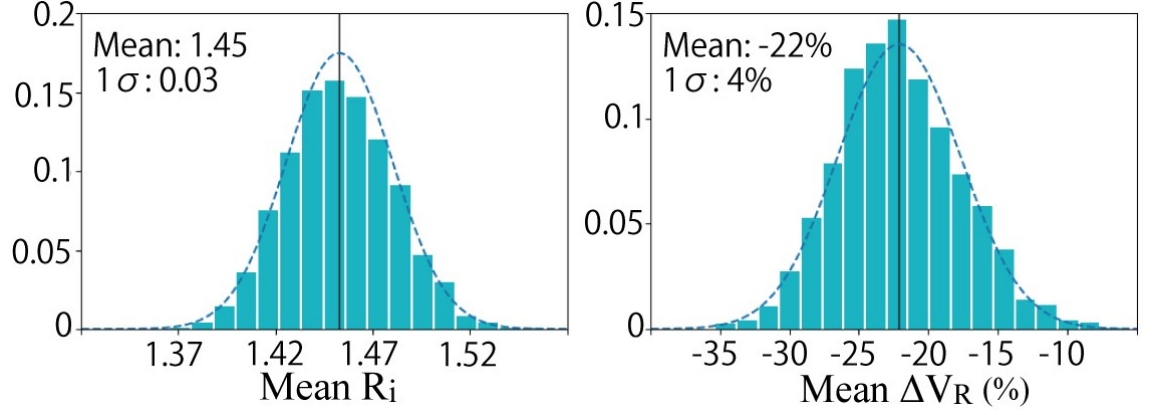
22

**Fig. 11.** Histograms of mean $R_i$ for DP3 quartz particles and mean $\Delta V_R$ obtained by the bootstrap method. In both histograms, the vertical axis represents the relative frequency.

3.4 Deformation analysis using the deformed vein sets method

In this study, the quartz veins developed in metagraywacke were used to estimate the deformation parameters. The deformed vein data were collected from five different sites (DP2, DP3, DP28 & 98DP5 on Fig. 9). Therefore, the estimated values of deformation parameters are representative of the deformation in the study area. The obtained deformed vein data are presented in table 2 and the data are plotted on a circle (Fig. 12).

**Table 2.** Data on the angle and type of shape of the deformed veins obtained from the field.

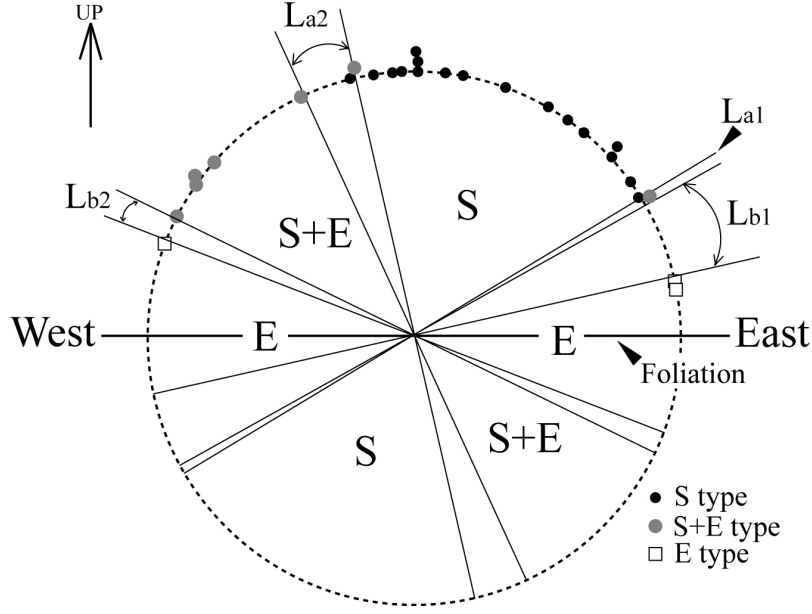|     | **Type** |     | **Type** |     | **Type** |
| --- | --- | --- | --- | --- | --- |
| 10  | E   | 60  | S   | 100 | S   |
| 12  | E   | 70  | S   | 104 | S+E |
| 29  | S+E | 80  | S   | 106 | S   |
| 30  | S   | 83  | S   | 116 | S+E |
| 35  | S   | 90  | S   | 140 | S+E |
| 42  | S   | 90  | S   | 145 | S+E |
| 42  | S   | 90  | S   | 146 | S+E |
| 50  | S   | 94  | S   | 154 | S+E |
| 55  | S   | 96  | S   | 160 | E   |

23

**Fig. 12.** Deformed vein data obtained in field.

The data shows that the angles of $L_{ai}$ and $L_{bi}$ measured counterclockwise from the foliation are in the following ranges:

$La_1 = 30°$,

$103° \leq La_2 \leq 116°$,

$12° \leq Lb_1 \leq 28°$, and

$155° \leq Lb_2 \leq 160°$.

We used our newly developed method to estimate constraints on the deformation parameters based on the field data. First, the range of deformation parameters is expressed using random numbers and a uniform distribution. This result shows the entire range of deformation parameters constrained from the field data. The volume change was estimated by using the average rotation value ($W_m = 0.72$) obtained by the analysis (Fig. 13). By using a normal distribution and random numbers, it is possible to indicate the range most likely for the deformation parameters, and so estimate appropriate uncertainties. In this case, the greatest density of points on the plot is approximately at the average position on the plot. The volume change was estimated using the average rotation value ($W_m = 0.72$) obtained by the analysis (Fig. 14).

Summarizing these results, it can be said that deformation was associated with a high degree of non-coaxiality. The foliation in this region has an east-west strike and a high-angle northward dip, and the mean vorticity number is positive (counterclockwise), implying a top to the west sense of shear. Our volume change

24

estimates are compatible with volume change from negligible to an increase of around 60% (Table 3). The results are not compatible with the large volume reduction proposed by earlier studies of this area (Ring, 2008).
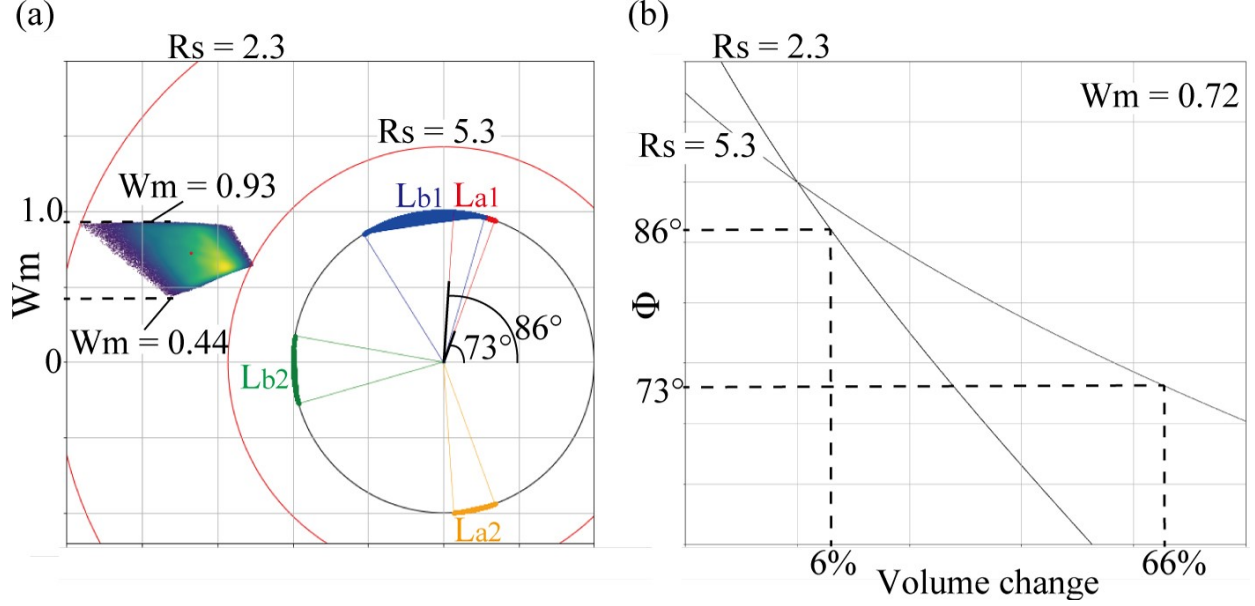


**Fig. 13.** The result of the analysis using uniform distribution for $L_{ai}$ and $L_{bi}$. (a): Mohr diagram, where the fine dots plotted in Mohr space represent the distribution of the deformation parameters for each Monte Carlo trial (N=100000). The lighter the color, the more points are plotted. (b): Graph of the relationship between the distribution range $\Phi$ and the volume change of $L_{ai}$. Using the upper and lower limits of the estimated range of $R_S$ and the mean $W_m$, a curve showing the relationship between $\Phi$ and volume change is obtained.
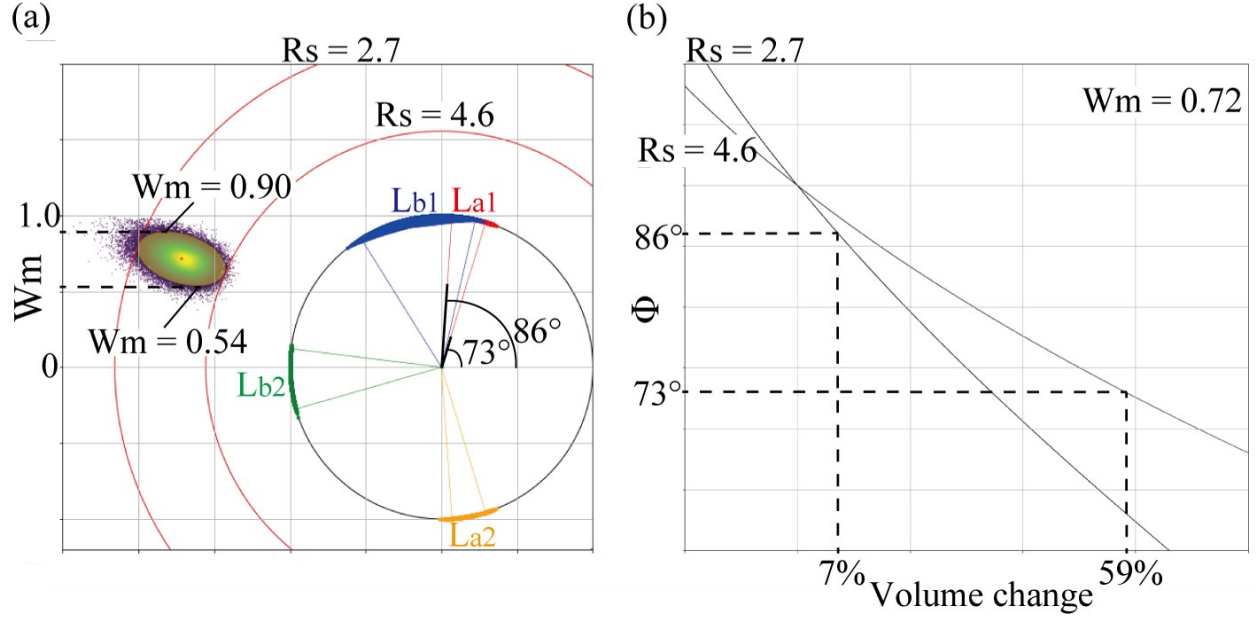
**Fig. 14.** The result of the analysis using normal distribution for $L_{ai}$ and $L_{bi}$. (a): Mohr diagram, where the fine dots plotted in Mohr space represent the distribution of the deformation parameters for each Monte Carlo trial (N=100000). The lighter the color, the greater the density of plotted points. The distribution of the dots can be approximated to a two-dimensional normal distribution. The overlaid yellow ellipse indicates the region containing 95% of the dots. (b): Graph of the relationship between the distribution range $\Phi$ and the volume change indicated by $L_{ai}$.

**Table 3.** The results of the deformed vein sets method.

| Distribution for $L_{ai}$ and $L_{bi}$ | $R_S$ | $R_S$ (mean) | $W_m$ | $W_m$ (mean) | $\Delta V$ | $\Delta V$(mean) |
|---|---|---|---|---|---|---|
| Uniform | 2.3–5.3 | 3.3 | 0.44–0.93 | 0.72 | 6%–66% | 27% |
| Normal | 2.7–4.6 | 3.3 | 0.54–0.90 | 0.72 | 7%–59% | 26% |

4 Discussion

4.1 Effects of non-passive marker behavior of veins

The deformed vein sets method assumes that the deformation of the mineral veins is directly reflected by folding, necking and boudinage of the veins. However, when the viscosity ratio between the mineral vein and the host rock is small, part of the shortening is absorbed by the thickening of the vein with no folding, and conversely, when the viscosity ratio is large, elongation of the folded vein may be partially absorbed by the opening of the hinge of the fold. A complete mechanical analysis of the response of mineral veins to an applied

deformation field is a complex problem. However, simpler considerations can be used to examine if the estimates from our approach presented above are lower or upper bounds.

An effective viscosity ratio between veins and the surrounding rock can be derived from the wavelength/thickness ratio for folded veins (Biot, 1961). The veins analyzed in this study show wavelength/thickness ratios of ~6.4 implying a low to moderate viscosity ratio of ~10. This means that unfolding will be limited and there will be little influence on the estimated location of $L_{ai}$. There is more likely to be layer-parallel shortening without folding and this will affect the estimated location of $L_{bi}$. The estimates of volume change depend on the location of $L_{ai}$ and finite strain, $R_f$. $R_f$ is known independently of the vein analysis so we conclude the influence of unfolding on volume change estimates will be limited. Changes in the location of $L_{bi}$ due to layer parallel shortening should affect the estimates of finite strain. However, the estimates of finite strain ratio using both the deformed vein analysis and independent $R_f/$ methods are in agreement within the uncertainties suggesting that the influence of layer parallel shortening results in uncertainties that are significantly smaller than those associated with the current data set.

4.2 Effect of Non-Steady-State Flow

Our analysis assumes steady flow. Natural deformation may deviate from this simple type of deformation history. To examine the effects of unsteady flow, we examine a geologically reasonable scenario in which early deformation near the plate boundary is dominated by simple shear, whereas later deformation has a greater component of pure shear as the rock moves away from the plate boundary during exhumation. In this case, applying our method to the predicted distribution and types of deformed veins would indicate an apparent volume increase greater than the real value. However, in this scenario there will always be a region of veins that have been shortened after being elongated (E + S vein types). This region is characterized by veins that are folded after being boudinaged. Since E + S type veins were not observed in this region, we consider the effect of non-steady flow in this case is limited.

4.3 Constraints on volume change based on observation of microstructure

Our deformed vein analysis suggests a minimum 7% volume increase in the study region. The upper limit from the same vein analysis is around 60%. Because $SiO_2$ is the most easily transported common chemical species in the sediments, such a large volume increase should be reflected in an unusual mineralogy and in particular in very quartz-rich lithologies. Such unusually quartz-rich lithologies are not observed. In addition, for significant volume increase all clastic grains should develop rims of extra added quartz. Any volume increase greater than the shortening due to finite strain should be recorded as a continuous rim around the clasts. In the examined samples limited overgrowths are observed restricted to the extension direction and none were observed on surfaces perpendicular to the Z direction of finite strain (Fig. 15). We conclude that any volume increase

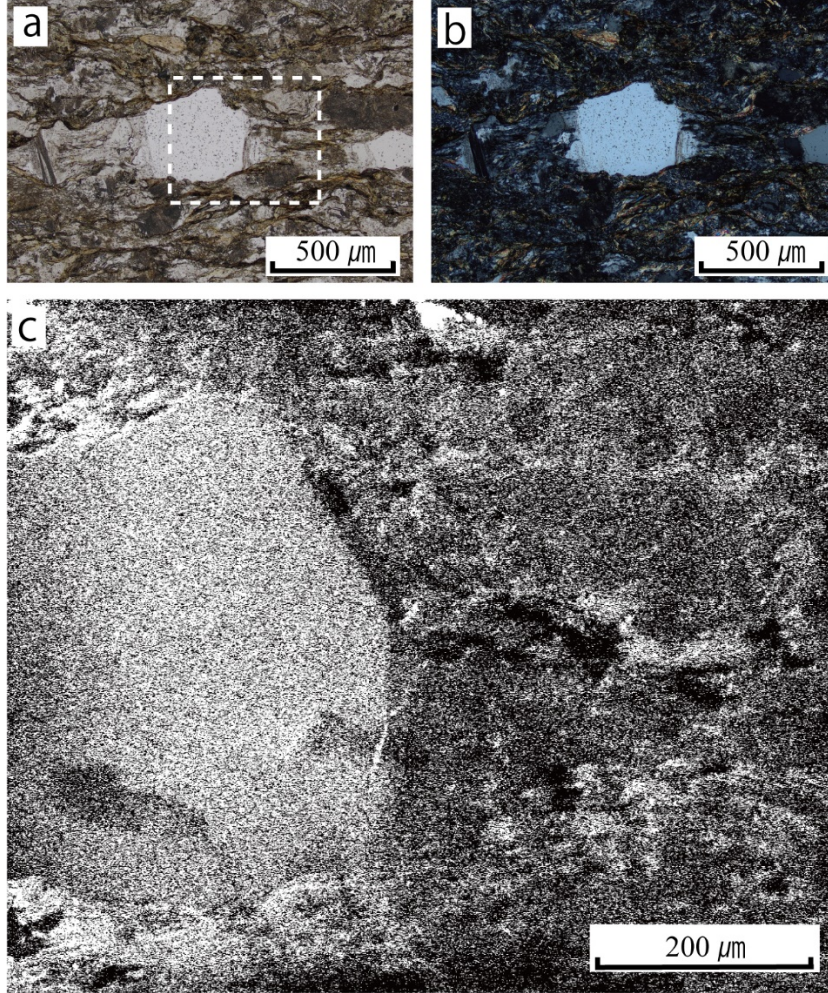has to be significantly less than the estimates of shortening along Z, i.e. $< 40\%$.



**Fig. 15.** Photomicrographs & CL image in XZ sections of a metagreywake sample. a: an image viewed in plane-polarized light, b: in cross polarized light. c: a cathodoluminescence image (the area within the dashed line in a). Clastic quartz grains are associated with pressure fringes of quartz.

4.4 Differences in Strain Estimates and Influence of Grain Boundary Sliding

The results of our strain analysis using the $R_f$ / method are significantly different for sandstone fragments and individual clastic quartz grains. Both strain markers record deformation through all periods from subduction to exhumation and the difference is, therefore, not due to different deformation histories. The most likely explanation for the differences in apparent strain is that the domains of quartz grains have accommodated strain in a way that is not reflected

in a change of shape. This is possible if grain boundary sliding occurs. Grain boundary sliding requires an accommodation mechanism to fill the voids that open as grain slide past one another. In the absence of dislocation creep, the two possible mechanisms are diffusion or solution transfer of mobile chemical species assisted by fluid flow. Both diffusion and percolative fluid flow along the grain boundaries become more difficult to achieve for greater length scales and so large particles are less likely to be affected by sliding along their boundaries and more likely to undergo internal deformation. Therefore, we consider the difference in the shortening recorded by the sandstone fragments and quartz particles represents the amount of shortening accommodated by grain boundary sliding on the grain scale, which here is about 10% (Fig. 16).

4.5 Stage of Recorded Deformation

The results of the deformed vein sets method show a shortening of 39–53% (Table 4). Deformed veins are developed on a cm–m scale and record strain due to both deformation of the constituent grains of the rock and grain boundary sliding and the results should be comparable to the sandstone fragments. A significant difference in the potential of veins and detrital sedimentary fragments to record deformation is related to their timing of formation. The presence of high P minerals in the veins shows the vein sets formed close to peak metamorphic conditions and their deformation does not record the prograde burial history. In contrast, the sedimentary fragments are part of the original rock and should record deformation developed throughout both subduction and exhumation phases. In other words, any difference between the strains recorded by the sandstone fragments and the deformed vein sets can be used as an estimate of the ductile strain developed during subduction. The analysis of the sandstone fragments and the deformed vein sets shows that there is no significant difference in their respective shortening, suggesting that the ductile deformation during subduction was very small compared to that developed close to peak metamorphic conditions and during exhumation. This result is compatible with the observation that only a single phase of ductile deformation is recorded in the mesofabrics of the metagreywake in this area.

**Table 4.** The results of the deformed vein sets method using a normal distribution for uncertainties. $R_S$ represents the axial ratio of the strain ellipse and indicates the range that is statistically compatible with the data at the 95%CI. *Indicates the maximum likelihood value of the result.

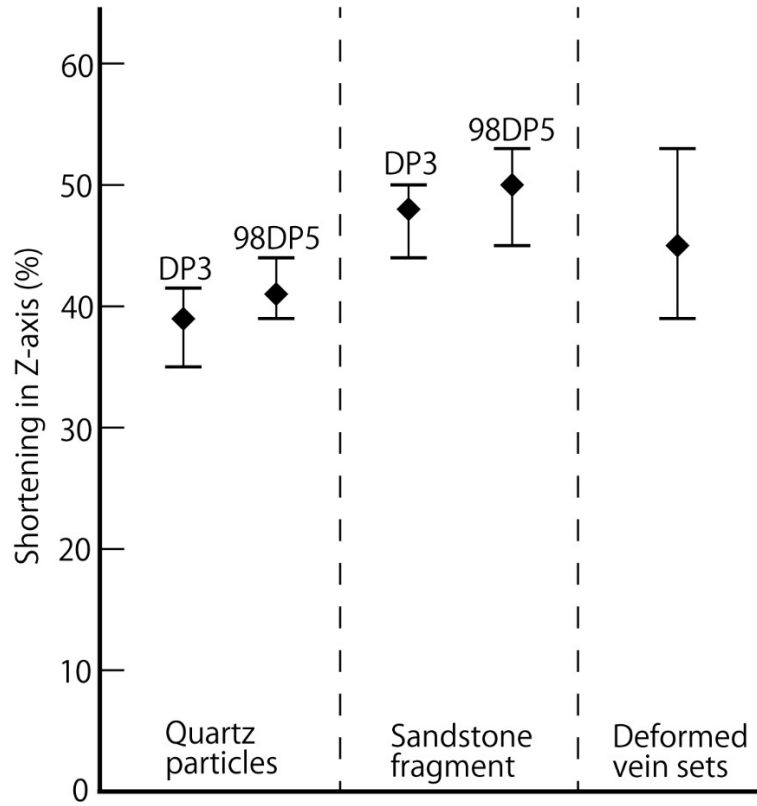| Deformed vein sets | | | | |
| --- | --- | --- | --- | --- |
| Scale of veins | Rs | Rs* | Shortening in Z-axis (%) | Shortening in Z-axis* (%) |
| cm–m | 2.7–4.6 | 3.3 | 39–53 | 45 |

**Fig. 16.** Comparison of estimates of shortening along the Z-axis from analyses of quartz grains, sandstone fragments and deformed vein sets. The error bars in the results for quartz particles and sandstone fragments represent the range that is statistically compatible with the data at the 5% significance level, while the error bars for the deformed vein sets represent the range that is statistically compatible with the data with 95% CI. The square plots represent the maximum likelihood estimates for each.

4.6 Grain Boundary Sliding and Discrepancy with Previous Studies

The analyses presented above yield an estimate of volume increase of 7–40%. This range is large, but is in stark contrast with previous estimates in the same area of a volume *decrease* of about 30% based on observations of quartz particles deformed by pressure dissolution and precipitation processes (Ring, 2008). Ring (2008) also estimated other deformation parameters and reported a finite strain ($R_S$) of 1.3 and a mean vorticity number ($W_m$) of 0.4. To compare the two sets of results, we calculated the expected distribution of deformed vein sets for the parameters proposed by Ring (2008) (Fig 17). The expected pattern of deformed vein types and their orientations is clearly inconsistent with our field data.
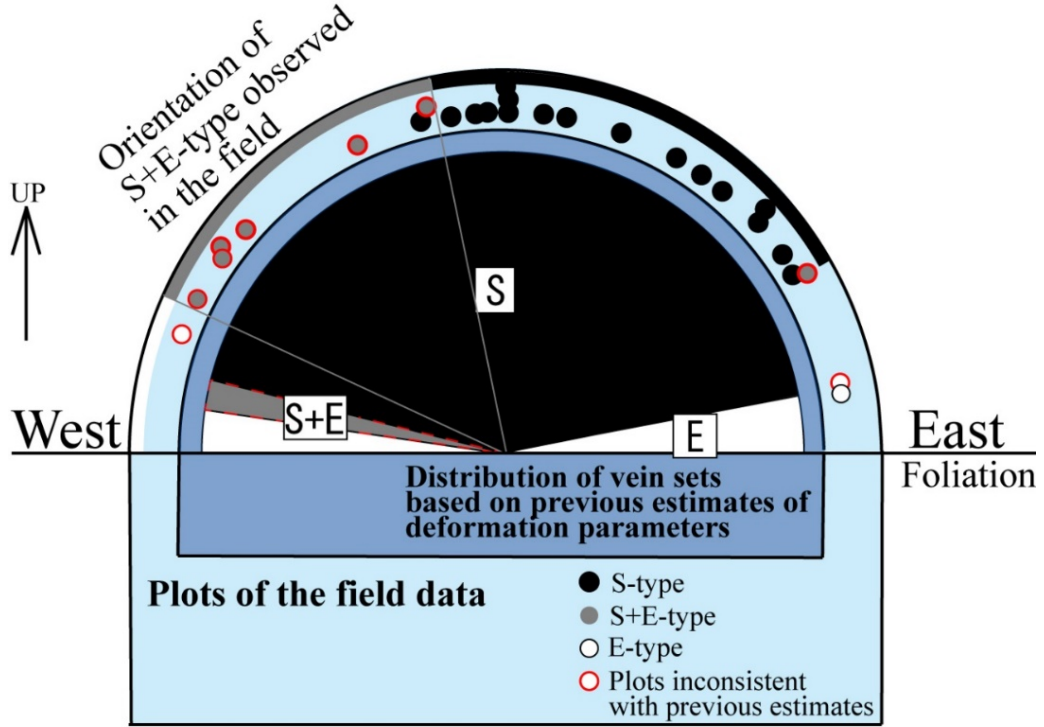
**Fig. 17.** Orientation patterns of the deformed vein sets assumed from the deformation parameters proposed by Ring (2008). The small circle plots represent the actual orientation data obtained in the field. Many of these data are inconsistent with the orientations expected based on the deformation parameters estimated by previous studies—the observed distribution of the S+E-type field shows a particularly clear discrepancy.

A significant potential problem with the method used by Ring (2008) to estimate deformation parameters is that the grain-scale analysis does not incorporate the possible influence of grain boundary sliding. Ring (2008) used the projected dimension strain (PDS) and mode methods (Brandon et al. 1994; Feehan & Brandon 1999) to measure contractional and extensional strains, respectively. He then used the maximum projected dimension (MPD) of the crystal in the X-direction as the reference frame for absolute stretching. MPD is commonly referred to as the Caliper dimension and refers to the length of a 3D particle as measured by calipers along a specific direction. Ring (2008) considered that the length of the crystal in the X-direction does not change when there is no internal strain in the crystal, based on the observation that the pressure solution proceeds through a mass transfer process at the grain boundary. Ring (2008)

further assumes that grains were originally randomly oriented and deform solely by pressure dissolution creep without rotation. In that case, the mean MPD $(X_g)$ in the X-direction of the grains is equal to the pre-deformation mean length in the X and Z directions, referred to as $X_1$ and $Z_1$. Based on these assumptions, the absolute shortening $(s_z)$ can be estimated by dividing the mean MPD $(Z_g)$ of the particles in the Z-direction by $X_g$. The absolute elongation $(s_x)$ can then be obtained by measuring the modal abundance (m) of fiber and grain in the X-direction. However, if grain rotation occurs associated with grain boundary sliding, the long axes of grains will be become reoriented towards the X-direction without an associated change in shape. This means that the measured $X_g$ will be greater than the true extension, causing an overestimation of the true shortening $(s_z)$. In the case of plane strain, the volume change ($\Delta$V) is expressed by $\Delta$V $= s_x \, s_z \, - 1$, and the bias caused by not incorporating grain rotation causes a systematic underestimation of the volume change. The maximum effect of rigid body rotation of individual grains on the estimates volume change can be estimated by assuming all grains become aligned with their long axes parallel to the maximum extension direction. In this case the amount of shortening in the Z direction is reduced by an amount equivalent to the mean aspect ratio of the grains $(R_r)$ calculated from the mean MPD in the X-direction $(X'_1)$ and the mean MPD in the Z-direction $(Z'_1)$ (Fig. 18).

Then

$$\Delta \mathrm{V}_{\mathrm{true}} = s_x \bullet s_z \, R_r$$

substitute $\Delta V_R = s_x \, s_z \, - 1$ (from above) and we obtain

$$V_{\mathrm{true}} = (1 + \ V_R) \, R_r - 1 \qquad\qquad (37)$$

Where $\Delta V_{\mathrm{true}}$ = true volume change, $\Delta V_R$ = volume change estimated by the method of Ring (2008), and $R_r = X'_1/Z'_1$.

**(a) Elements of deformation assumed in Ring (2008)**

**(b) Elements of deformation assumed in this paper**



Alignment of grains by rigid body rotation (with no change of shape & volume)

Shape change of grains by solution mass transfer without rigid body rotation (related to volume change)

Shape change of grains by solution mass transfer (related to volume change)

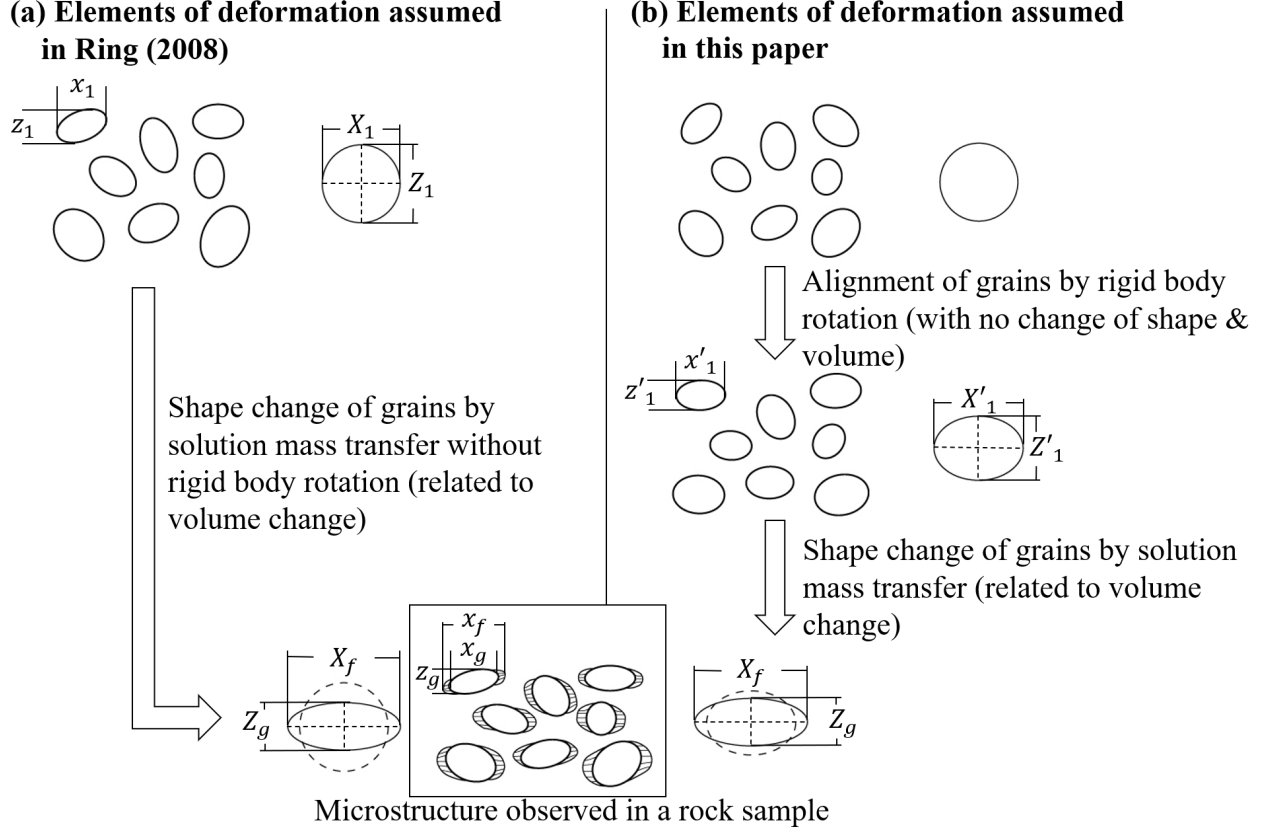Microstructure observed in a rock sample

**Fig. 18.** Comparison between the deformation process assumed by Ring (2008) and those used in this paper. In both cases, the initial conditions are randomly oriented ellipsoidal grains of arbitrary shape and the average lengths of grains in the X and Z directions are equal. The final result is the same in both cases. Both approaches assume that the length of the grains in the X direction (excluding the fiber) does not change during solution mass transfer, so $x_g = x_1 = x'_1$. These are used as reference frames for length changes. The main difference between the two processes is that the shortening in the Z direction associated with the volume change is $Z_g/Z_1$ in (a) and $Z_g/Z'_1$ in (b). $Z_1 > Z'_1$ implying that the shortening is overestimated in (a), where rigid body rotation is ignored.

4.7 Volume change in the Del Puerto Canyon region

Combining the results of the Rf/  and bootstrap methods suggests that the 1  range of the mean initial aspect ratio of the grains before deformation ($R_i$) is 1.42–1.48. We used this result and the bootstrap analysis to estimate a 1  range of $-27\%$ – $-18\%$ for the apparent volume change given by Ring (2008). Calculating the volume change using equation (37) based on our maximum estimate of $R_i = 1.48$ and the lower estimate of volume decrease from the Ring (2008) method of $\Delta V = -18\%$ yields a maximum value of the true volume

increase, $\Delta V_{\mathrm{true}}$, of 21%. Since $R_i$ is the maximum value that $R_r$ can take, the 21% volume increase is an upper limit for the estimation of volume change in this region. Also, the results of our deformed vein sets method shows a 7% increase in volume as a lower limit. Therefore, we conclude that appropriate bounds for the volume change in this region are a volume increase of 7–21%. This range is similar to the amount of silica addition that has been proposed based on seismic velocity studies (Audet, P. & Burgmann, R., 2014) and may help account for time scales of slow slip events.

5 Conclusions

(1) The Variable-origin Mohr diagram for finite deformation with a movable origin and fixed radius is proposed here as a useful tool for estimating the deformation parameters, and identifying suitable uncertainties associated with kinematic analysis using deformed veins sets.

(2) The key angle (between lines $L_{a1}$ and $L_{a2}$) for estimating volume change is determined almost entirely by finite strain and volume change with little influence by the rotational component. Estimates of volume change from the deformed vein set method can be improved by combining them with independent estimates of finite strain.

(3) A comparison of strain estimates by different methods suggests that the strain of metagraywacke in the Del Puerto Canyon region of the Franciscan metamorphic belt is accommodated not only by shape changes of the constituent mineral grains but also by sliding along the grain boundaries and about 10% of the shortening in the Z-axis direction is due to this grain boundary sliding. A comparison between the results of the deformed vein sets method and the Rf / strain analysis that uses sandstone fragments allows the strain developed during subduction and exhumation to be separated; in this case the deformation during subduction is very small compared to that during exhumation.

(4) A combination of the results of the deformed vein sets method and thin section observations suggests volume increase in this region of greater than 7%. A consideration of the effects of grain rigid-body rotation combined with the microstructural observations of Ring (2008) yields an upper limit for the volume increase of 21%. This implies that 7–21 vol.% of the rock now observed was added to this region by precipitation from fluid derived from a deeper region. Such a volume increase is compatible with estimates for some convergent margins based on seismic observations.

**Open Research**

The Jupyter Notebook to execute the analysis in the paper can be found at https://mybinder.org/v2/zenodo/10.5281/zenodo.5907771/, is hosted at GitHub and is preserved at https://doi.org/10.5281/zenodo.5907771, v1.0.0, open.

**References**

Audet, P. & Burgmann, R., 2014. Possible control of subduction zone slow-earthquake periodicity by silica enrichment. *Nature,* **510**, 389–392.

Beutnr. E. C. & Charles, E. G. 1985. Large volume loss during cleavage formation, Hamburg sequence, Pennsylvania. *Geology*, **13**, 803–805.

Bhagat, S. S. & Marshak, S., 1990. Microlithon alteration associated with development of solution cleavage in argillaceous limestone: textural, trace-elemental and stable isotope observations. *Journal of Structural Geology*, **12**, 3944.

Biot, M. A., 1961, Theory of folding of stratified viscoelastic media and its implications in tectonics and orogenesis. *Geol. Soc. America Bull.*, **72** (11), 1595–1620.

Brandon, M. T., Cowan, D. S., & Feehan, J. G., 1994. Fault-zone structures and solution-mass-transfer cleavage in Late Cretaceous nappes, San Juan Islands, Washington. In *Geologic Field Trips in the Pacific Northwest: Geological Society of America 1994 Annual Meeting* (Vol. 2, pp. 1–19). Seattle: Dep. of Geol. Sci., Univ. of Wash.

Bray, C.J. & Karig, D.E., 1985. Porosity of sediments in accretionary prisms and some implications for dewatering processes. *Journal of Geophysical Research*, **90** (NB1), 768–778.

Breeding, C. M. & Ague, J. J., 2002. Slab-derived fluids and quartz-vein formation in an accretionary prism, Otago Schist, New Zealand. *Geology*, **30**, 499–502.

Ernst, W.G., 1993, Metamorphism of Franciscan tectonostratigraphic assemblage, Pacheco Pass area, east-central Diablo Range, California Coast Ranges. *Geological Society of America Bulletin*, **105**, 618–636.

Erslev, E.A. & Ward, D. J., 1994. Non-volatile element and volume flux in coalesced slaty cleavage. *Journal of Structural Geology*, **16**, 531–553.

Evarts, R. C., 1977. The geology and petrology of the Del Puerto Ophiolite, Diablo Range, Central California Coast Ranges, in Coleman, R. G., and Irwin, W. P., eds., North American ophiolites: *Oregon Department of Geology and Mineral Resources Bulletin*, **95**, 121–139.

Feehan, J. G., & Brandon, M. T., 1999. Contribution of ductile flow to exhumation of low-temperature, high-pressure metamorphic rocks: San

Juan-Cascade nappes, NW Washington State. *Journal of Geophysical Research: Solid Earth*, **104**(B5), 10883–10902.

Ghosh, S.K. & Ramberg, H., 1976. Reorientation of inclusions by combination of pure shear and simple shear. *Tectonophysics*, **34**, 1–70.

Grant, J.A., 1986. The isocon diagram e a simple solution to Gresens equation for Metasomatic alteration. *Economic Geology*, **81** (8), 1976–1982.

Gresens, R., 1967. Composition-volume relationships of metasomatism. *Chemical Geology*, **2**, 47–65.

Kawabata, K., Tanaka, H. & Kimura, G., 2007, Mass transfer and pressure solution in deformed shale of accretionary complex: Examples from the Shimanto Belt, southwestern Japan. *Journal of Structural Geology*, **29**, 697–711.

Lindeberg, J. W., 1922. Eine neue Herleitung des Exponentialgesetzes in der Wahrscheinlichkeitsrechnung. *Mathematische Zeitschrift*, **15**(1), 211–225.

Lisle R. J., 1985. Geological strain analysis: a manual for the Rf- technique, p. 99. A. Wheaton, Exeter.

Lister, G.S., Williams, P.F., 1983. The partitioning of deformation in flowing rock masses. *Tectonophysics*, **92**, 1–33.

MacKenzie, D. P., 1979. Finite deformation during fluid flow. *Geophys. J. R. Astron. Soc.*, **58**, 689–715.Malvern, L. E., 1969. *Introduction to the Mechanics of a Continuous Medium.* Prentice-Hall, Englewood Cliffs, New Jersey.

McLennan, S.M. & Taylor, S.R., 1996, Heat flow and the chemical composition of continental crust. *Journal of Geology*, **104**, 369–377.

Means, W. D., 1982. An unfamiliar Mohr circle construction for finite strain. *Tectonophysics*, **89**, TI–T6.

Means, W. D., 1983. Application of the Mohr-circle construction to problems of inhomogeneous deformation. *Journal of Structural Geology*, **5**, 279–286.

Moriyama, Y., & Wallis, S., 2002. Three-dimensional finite strain analysis in the high-grade part of the Sanbagawa Belt using deformed meta-conglomerate. *Island Arc*, **11**(2), 111–121.

Passchier, C.W., 1987. Stable positions of rigid objects in non-coaxial flow e a study in vorticity analysis. *Journal of Structural Geology*, **9**, 679–690.

Passchier, C. W., 1988. The use of Mohr circles to describe noncoaxial progressive deformation. *Tectonophysics*, **149**, 323–338.

Passchier, C. W., 1990. Reconstruction of deformation and flow parameters from deformed vein sets. *Tectonophysics*, **180**, 185–199.

Passchier, C.W., 1993. The sliding-scale Mohr diagram. *Tectonophysics*, **218**, 367–373.

Patrick, B.E. & Day, H.W., 1989. Controls on the first appearance of jadeitic pyroxene, northern Diablo Range, California. *Journal of Metamorphic Geology*, **7**, 629–639.

Platt, J. P., Xia, H. & Schmidt, W. L., 2018. Rheology and stress in subduction zones around the aseismic/seismic transition. *Prog. Earth. Planet. Sci*, **5**(1): 24.

Ramsay J. G., 1967. Folding and Fracturing of Rocks. *McGraw-Hill, New York*, 568.

Ramsay, J. G. & Huber, M. I., 1983. The Techniques of Modern Structural Geology, Volume 1: Strain Analysis. *Academic Press, New York.*

Ring, U., 2008. Deformation and Exhumation at Convergent Margins: The Franciscan Subduction Complex. *The Geological Society of America, Special paper*, 445

Ring, U. & Brandon, M.T., 1999. Ductile Deformation and Mass Loss in the Franciscan Subduction Complex: Implications for Exhumation Processes in Accretionary Wedge. Exhumation Processes: Normal Faulting, Ductile Flow and Erosion. *Geological Society, London, Special Publications.*

Saffer, D. M. & Tobin, H. J. 2011. Hydrogeology and Mechanics of Subduction Zone Forearcs: Fluid Flow and Pore Pressure. *Annu. Rev. Earth Planet. Sci.*, **39**, 157–86.

Soejima, S. 2022. shogosoejima/ss_repository: Python program for estimating volume change of rocks (v1.0.0). Zenodo. https://doi.org/10.5281/zenodo.5907771

Talbot, C. J. 1970. The minimum strain ellipsoid using deformed quartz veins. *Tectonophysics*, **9**, 46–76.

Tan, B.K., Gray, D.R. & Stewart, I. 1995. Volume change accompanying cleavage development in graptolite shales from Gisborne, Victoria, Australia. *Journal of Structural Geology*, **17**, 1387–1394.

Tikoff, B., Fossen, H., 1995. The limitations of three-dimensional kinematic vorticity analysis. *Journal of Structural Geology*, **17**, 1771–1784.

Wallis S. R. 1992. Vorticity analysis in a metachert from the Sanbagawa belt SW Japan. *Journal of Structural Geology*, **14**, 271–80.

Wallis S. R. 1995. Vorticity analysis and recognition of ductile extension in the Sanbagawa belt, SW Japan. *Journal of Structural Geology*, **17**, 1077–1093.

Wallis, S.R., Platt, J.P. and Knott, S.D., 1993. Recognition of syn-convergence extension in accretionary wedges with examples from the Calabrian Arc and the Eastern Alps. *American Journal of Science*, **293**(5), 463-494.

Wintsch, R. P., Kvale, C. M. & Kisch, H. J. 1991. Open-system. constant-volume development of slaty cleavage, and strain induced replacement reactions

in the Martinsburg Formation, Lehigh Gap, Pennsylvania. *Geological Society of America Bulletin*, **103**, 916–927.

Wood, D.S. (1973) Patterns and magnitudes of natural strain in rocks. *Philosophical Transactions of the Royal Society, London*, **A274**, 373–382.

Wood, D.S. (1974) Current views on the development of slaty cleavage. *Annual Review of Earth and Planetary Sciences*, **2**, 122–135.

Wright, T. O. & Henderson, J. R. 1992. Volume loss during cleavage formation in the Meguma Group, Nova Scotia. Canada. *Journal of Structural Geology*, **14**, 281–290.

Wright, T. O. & Platt, L. B. 1982. Pressure dissolution and cleavage in the Martinsburg Shale. *American Journal of Science*, **282**, 122–135.